Electron transfer dynamics across self-assembled *N*-(2-mercaptoethyl) octadecanamide/mycolic acid layers: impedimetric insights into the structural integrity and interaction with anti-mycolic acid antibodies†

Kenneth I. Ozoemena,*[ab] Nsovo S. Mathebula,[b] Jeseelan Pillay,[b] Gianna Toschi[b] and Jan A. Verschoor[c]

Received 4th August 2009, Accepted 14th October 2009
First published as an Advance Article on the web 12th November 2009
DOI: 10.1039/b915930d

The integrity and properties of mycolic acid (MA) antigens integrated into a self-assembled monolayer (SAM) of *N*-(2-mercaptoethyl)octadecanamide, (MEODA), on a gold electrode have been interrogated using cyclic voltammetry (CV) and electrochemical impedance spectroscopy (EIS). EIS data showed that Au–MEODA and Au–MEODA–MA behave as microelectrode arrays, with pinholes acting as the microelectrodes that permit electron transport between a redox-active probe in solution and the underlying gold surface. The average radii of the pinholes (r_a) and half the distance between the centers of the neighbouring pinholes (r_b), were estimated from EIS using the pore size model, and discussed. Anti-MA antibodies present in a tuberculosis (TB)-infected patient (co-infected with HIV) strongly interact with Au–MEODA–MA showing a rather compact and stable bio-complex structure that is virtually defect-free. The electrochemical impedimetric properties associated with the ability of the Au–MEODA–MA to discriminate between TB positive and negative human sera are also discussed. We prove that the Au–MEODA and Au–MEODA–MA electrodes, as well as the MA-anti-MA antibody interactions, are characterized with time-constant dispersion, typical of microstructures with grain/grain boundary phases. These crucial physico-electrochemical insights into the behaviour of surface-confined MA should provide a useful basis for the design and development of a potential impedimetric immunosensing platform for active tuberculosis.

1. Introduction

Mycolic acids (MA, Fig. 1) are long-chain (C_{60}–C_{90}), high molecular weight α-alkyl-β-hydroxy fatty acids that constitute the major chemical components of the cell walls of *Mycobacterium tuberculosis* (*M. tuberculosis*) and related organisms.[1] MA consists of two characteristic parts, the mycolic motif and the mero-chain, of which the latter varies in stereochemistry and spacing of its two functional groups. On the basis of these differences on the mero-chain, MA of *M. tuberculosis* are sub-divided into subclasses, namely alpha-, methoxy- and keto-mycolate. Antibodies to free MA have been shown to be potential surrogate markers for the serodiagnosis of tuberculosis (TB).[2,3] TB remains the major cause of death in the world, with 2 million deaths and 9 million new cases per year.[4] In HIV/AIDS co-infected individuals,[5] it has been estimated that a delay of three to four weeks in the diagnosis and subsequent treatment of TB upon day of presentation accounts for 45–85% of deaths in TB/HIV co-infected patients.[6]

Importantly, it is known that irrespective of the level of severity of the immune deficiency measured by the fall of the CD4 T cell count, HIV-TB co-infected patients maintain high antibody levels to MA antigens.[2] Unfortunately, however, one of the factors that strongly conspire against the use of free MA in serodiagnostic enzyme-linked immunosorbent assay (ELISA) of TB is low accuracy (57%).[2] ELISA techniques require extra enzyme-labeled antibodies and intense sample clean-up to operate, thus restricting its application for on-site testing. Also, no single ELISA test has succeeded as a reliable test to confirm TB. It is crucial to search for a more efficient

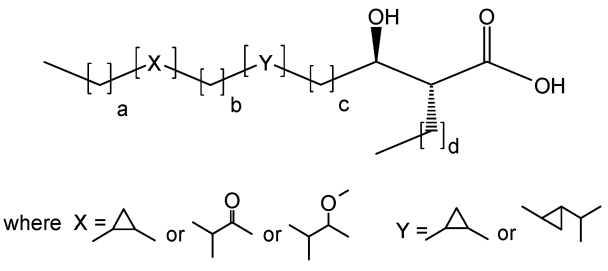

Fig. 1 Structural formula of mycolic acids. The letters a (15–19), b (10–16), c (11–21), d (21 or 23) depict the inter-chain lengths, which vary within and amongst mycobacterial species and X is a functional group which is unique to each subclass.

[a] *Materials Science and Manufacturing, Council for Scientific and Industrial Research (CSIR), Pretoria 0001, South Africa. E-mail: kozoemena@csir.co.za; Fax: +27 (0)12 841 2135; Tel: +27 (0)12 841 3664*
[b] *Department of Chemistry, University of Pretoria, Pretoria 0002, South Africa*
[c] *Department of Biochemistry, University of Pretoria, Pretoria 0002, South Africa*

† Electronic supplementary information (ESI) available: Core level XPS spectra of Au–MEODA. See DOI: 10.1039/b915930d

and cost-effective means of using MA antigens for sensitive diagnosis of TB especially in Sub-Saharan Africa where the population is most burdened by the HIV/AIDS pandemic.

One of the possible means of utilizing MA antigens for potential electrochemical serodiagnosis of TB is by devising a strategy for immobilizing them onto an electrode surface as an ultrathin film. Self-assembly has emerged as one of the elegant means of fabricating stable and well-organized arrays of ultrathin superstructure films of organothiolates on gold surfaces,[7–11] and used in electrochemical sensing. Since MA does not contain sulfur in its molecular structure for integration onto a gold electrode as a self-assembled monolayer (SAM), an alternative means of self-assembly that harnesses its hydrophobic character should be considered. Thus, in our recent short communication,[12] we reported that a SAM of *N*-(2-mercaptoethyl)octadecanamide (MEODA) could act as a hydrophobic support for integrating MA onto gold electrode and potentially be used for impedimetric recognition of anti-MA antibodies present in TB-positive serum. Viable fabrication and application of this SAM-based electrode as an electrochemical immunodiagnostic platform for TB will, however, require thorough understanding of the integrity and electrochemical properties of these gold-confined (MA and MEODA) species. This work is aimed at addressing this challenge using electrochemical impedance spectroscopy (EIS). EIS has become a very powerful non-destructive tool for probing properties of molecules at surfaces.[12–18] When compared to cyclic voltammetry (CV), EIS provides more detailed information on the chemistry occurring at the electrode/solution interface. EIS is a less perturbing electrochemical strategy since it is operated at smaller applied potential ($\leq$10 mV) compared to the CV, which is particularly very crucial to soft materials such as the biomolecular lipids investigated in this work. We prove that these gold-confined species (Au–MEODA–MA and Au–MEODA–MA/SAP) behave like microelectrode arrays, with the pinholes acting as the microelectrodes that permit electron transport between a redox-active probe in solution and the underlying gold surface. The size of the pinholes and the distance between the centers of the neighbouring pinholes are estimated and discussed. In addition, we show that the interaction between immobilized MA and anti-MA antibodies in TB positive serum exhibit the behaviour of time-constant dispersion, characteristic of microstructures with grain/grain boundary phases.

2. Experimental

2.1 Materials and reagents

Cysteamine hydrochloride (98% pure) and stearic acid (95%) were obtained from Sigma. Mycobacterial mycolic acids (MA) were isolated from a culture of *M. tuberculosis* H37Rv (American Type Culture Collection 27294) as previously described.[19] Human sera, collected for another study,[2] from the general medical wards of the Helen Joseph Hospital, Johannesburg (South Africa) were used; one tuberculosis and Human immunodeficiency virus-positive (HIV^+/TB^+) and one tuberculosis-negative and Human immunodeficiency virus-tuberculosis negative (HIV^-/TB^-) serum. The (HIV^+/TB^+) serum was from a patient with newly-diagnosed smear-positive active pulmonary tuberculosis who was not on anti-TB chemotherapy at the time of serum collection. The (HIV^-/TB^-) patient had a medical condition other than TB. Phosphate buffer saline solutions (PBS) were prepared with appropriate amounts of K_2HPO_4 and KH_2PO_4 containing 2.5 mM KCl and sodium azide 1 mM. Dicyclohexylcarbodiimide (DCC 99% pure) used as condensing agent was obtained from Aldrich. Saponin (blocking agent) was obtained from Sigma. *N*,*N*-Dimethylformamide (DMF) purchased from Sigma-Aldrich, was distilled and dried before use. Potassium hexacyanoferrate(II) ($K_4Fe(CN)_6$) was obtained from B. Jones Ltd., SA, potassium hexacyanoferric(III) ($K_3Fe(CN)_6$) was purchased from Bio-Zone Chemicals, SA. Ultra pure water of resistivity 18.2 MΩ cm was obtained from a Milli-Q Water System (Millipore Corp., Bedford, MA, USA) and was used throughout for the preparation of solutions. Phosphatidylcholine (PC) used for preparing liposomes was obtained from Sigma. All electrochemical experiments were performed with nitrogen-saturated PBS. All other reagents were of analytical grades and were used as received from the suppliers.

2.2 Apparatus and procedure

All electrochemical experiments were carried out using an Autolab Potentiostat PGSTAT 302 (Eco Chemie, Utrecht, Netherlands) driven by GPES and FRA software version 4.9). Electrochemical impedance spectroscopy (EIS) measurements were performed between 10 mHz and 10 kHz using a 5 mV rms sinusoidal modulation in a solution of 1 mM $K_4Fe(CN)_6$/$K_3Fe(CN)_6$ (1 : 1) mixture containing 0.1 M KCl, and at the $E_{1/2}$ of the $[Fe(CN)_6]^{3-/4-}$ (0.124 V *vs.* Ag|AgCl, sat'd KCl). The FRA software allowed the fitting of the raw EIS data to equivalent circuit models using a complex non-linear least squares (CNLS) routine, with the Krammers–Kronig rule check. Polycrystalline gold electrode (BAS, r = 0.8 mm) was used as the working electrode. Ag|AgCl sat'd KCl and platinum rod were used as reference and counter electrodes, respectively. All solutions were de-aerated by bubbling pure nitrogen (Afrox, South Africa) prior to each electrochemical experiment. All experiments were performed at 25 ± 1 °C. AFM images were obtained at SAM-modified SPR gold disks (Eco-Chemie) using an AFM 5100 System (Agilent Technologies, AC mode AFM scanner interfaced with a PicoScan controller, scan range 1.25 μm in x–y and 2.322 μm in z, silicon type PPP-NCH-20 (Nanosensors®) of thickness 4.0 ± 1.0 μm, length 125 ± 10 μm, width 30 ± 7.5 μm, spring constants 10–130 N m^{-1}, resonant frequencies of 204–497 kHz and tip height of 10-15 μm). All images (256 samples/line × 256 lines) were taken in air at room temperature and at scan rates 0.9–1.0 lines s^{-1}. The X-ray photoelectron spectra (XPS) were obtained at SAM-modified SPR gold disks using a Physical Electronics model 5400 spectrometer system with monochromatic Mg Kα radiation at 1253.6 eV at take-off angles of 151°.

2.3 Formation of SAMs and immobilization of mycolic acid antigens

Prior to modification, the gold electrode was cleaned as described before.[10,11,20] In brief, the gold electrode was first

polished with slurries of aluminium oxide nanopowder (Sigma-Aldrich), mirror finished on a Buehler felt pad and then subjected to ultrasonic vibration in ethanol to remove residual alumina nanopowder at the surface. Finally, the gold electrodes were then treated with 'Piranha' solution (1 : 3 (v/v) 30% H_2O_2 and concentrated H_2SO_4) for about 2 min; to remove organic contaminants and was followed by thorough rinsing with distilled water. To ensure that the gold electrode surface is clean, CV experiments were carried out with the electrode in 0.5 M H_2SO_4 and the potential scanned between −0.5 and 1.5 V at a scan rate of 50 mV s^{-1} until a reproducible CV scan was obtained. The real surface area of the bare gold electrode, determined from the reversible electrochemistry of $K_4Fe(CN)_6/K_3Fe(CN)_6$ as described before,[10,20] was 0.0257 cm^2 giving a surface roughness factor of 1.28 (ratio of real to geometrical surface area). Where applicable the real surface area was used for all calculations. As observed by Diao *et al.*,[21] impedance of different samples is not exactly the same even under the same experimental conditions possibly due to the surface states of the bare gold electrode that may differ from sample to sample. To reduce such uncertainties, in this work, one gold electrode was used to record a set of similar experiments.

The formation of the MEODA SAM on a clean polycrystalline gold electrode and the subsequent integration of the MA antigens on the SAM (herein abbreviated as Au–MEODA–MA) are summarized as shown in Scheme 1. Cysteamine SAM was first formed on clean gold surface as we described before[10,11] in nitrogen-saturated absolute ethanol solution of 10 mM Cysteamine for 18 h at ambient temperature, followed by covalent attachment of the stearic acid using the well established carbodiimide coupling chemistry in a stearic acid DMF–DCC solution to form an amide bond.[22] After the formation of the Au–MEODA SAM, the modified electrode was thoroughly rinsed in copious amounts of distilled deionised water and ethanol to remove physically adsorbed stearic acid species. The MA antigens were integrated into the MEODA SAM by incubating the electrode in dry DMF solution of MA (0.5 mg mL^{-1}) for about 48 h at room temperature. After the immobilisation of the MA antigens, the electrode was rinsed several times with PBS solution (pH 7.4) to remove the excess of physically bound MA species and immersed in 1.5 mg mL^{-1} PBS solution of saponin for 2 h to block nonspecific binding sites.

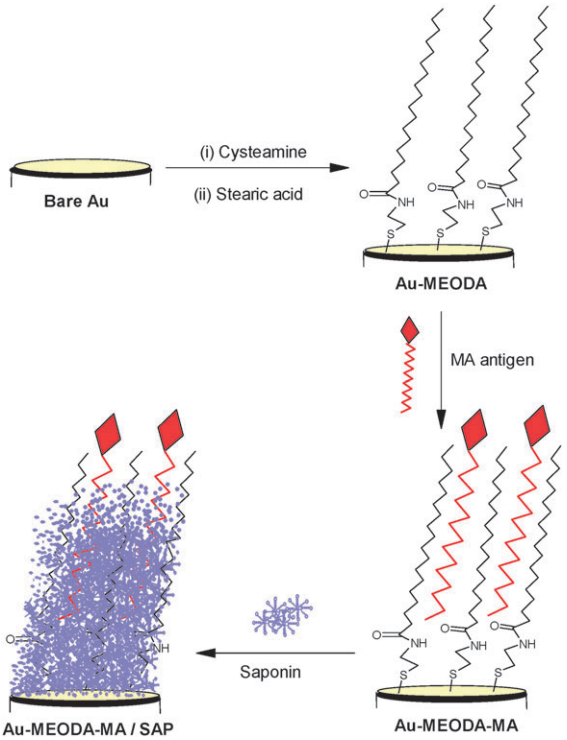

Scheme 1 Schematic of the modification steps of gold electrode with Au–MEODA–MA/SAP.

2.4 Preparation of liposomes and analysis of MA-anti-MA antibody interactions

Liposomes with and without mycolic acids (MA) were prepared from a phosphatidylcholine (PC)–$CHCl_3$ stock solution (100 mg ml^{-1}) as previously reported.[3,23] Briefly, MA-containing liposomes were prepared by mixing 90 μL of PC–$CHCl_3$ stock solution (100 mg ml^{-1}) with 1 mg of dried mycolic acids. Empty liposomes (*i.e.*, without MA) were prepared consisting of only PC–$CHCl_3$ solution. The PC–$CHCl_3$ contents in an amber glass vial were initially vortexed to ensure thorough mixing, dried at 85 °C (using a heat block) under a stream of pure nitrogen gas for about 10 min. Liposome formation was induced by addition of 2 ml of saline (0.9% NaCl) and placing in a heat block at 85 °C for 20 min, with vortexing every 5 min. The liposomes were then sonicated using a Branson sonifier (Model B-30, Branson Sonicator Co., USA) for 2 min at 30% duty cycle at an output of 3%. Subsequently, the liposomes were divided into 200 μl aliquots, freeze-dried and stored at −70 °C until ready for use. Before use, the liposomes were reconstituted with 2 ml of phosphate-buffered saline containing sodium azide (0.025%, m/v) and 1 mM EDTA (PBS–AE, pH 7.4), heated at 80 °C for 20 min and then sonicated as before. The final liposome concentration was 500 μg ml^{-1}.

Human sera (from TB-positive and TB-negative patients) were appropriately diluted in empty liposome PBS–AE (pH 7.4) (1 : 2000; 1 : 1000 and 1 : 500 v/v, *i.e.*, 0.05, 0.1 and 0.2% serum, respectively). For control experiments, similar procedure was followed using liposomes containing MA. The modified electrode (working electrode) was incubated in the required serum solution for 10 min, rinsed in a copious amount of PBS–AE (pH 7.4) to remove any physically adsorbed species before performing the EIS experiments.

Safety note. Piranha solution used in cleaning the gold surface reacts violently with organic materials and can explode when stored in closed containers. All glassware in contact with human sera (both TB positive and negative) must be sterilized for 1.5 h at 115 °C before and after use. Waste solutions must be carefully collected and sterilized before disposal. Intending workers must ensure they are vaccinated against hepatitis B.

3. Results and discussion

3.1 SAM fabrication, XPS and AFM characterization

The formation of each species on gold electrodes is summarized in Scheme 1. The initial process of *in situ* synthesis of MEODA using cysteamine and stearic acid *via* carbodiimide coupling chemistry was confirmed using XPS. The condensation of the –COOH functional groups of the stearic acid, activated by the DCC, with the $–NH_2$ groups of the Cys SAM resulted in the formation of the amide bonds. This type of covalent linkage using the carbodiimide coupling chemistry is well documented, for example, in linking enzymes and proteins to gold electrodes as SAMs.

X-Ray photoelectron spectroscopy studies were used to investigate the possible formation of a self assembled monolayer of cysteamine and the subsequent coupling of stearic acid to the cysteamine. Fig. 2 shows an example of X-ray photoelectron spectra data for Au-Cys and Au–MEODA obtained at a take-off angle (TOA) of 151°. The formation of the cysteamine SAM is evident by the gold-bound sulfur (Au–S) peak at 161.5 eV.[24–26] This peak appeared broad for the Au–MEODA due to reorganization processes in the film brought about by the formation of an amide bond between the gold bound cysteamine and stearic acid. Unlike the bare gold (not shown), the N atom peak is observed at 402 eV, confirming the attachment of the cysteamine and stearic acid *via* amide bond. Unlike the Au-Cys, the Au–MEODA gave well-resolved peaks at 285.1 eV signifying the presence of sp^3 carbon and 287.7 eV due to –C═O species arising from the amide bond. Also, unlike the Au-Cys SAM, the Au–MEODA gave an intense oxo-related peak at 536 eV, further confirming the presence of the amide bond.

Further experiments were performed to obtain the C (1s) and O (1s) core level spectra of the MEODA (see Fig. SI 1 in the ESI†). The multiplexing results showed three peaks for the main C (1s) spectrum at 284.09 eV ($C–H_2$), 285.74 eV (CH_2–NH), and at 287.47 eV (–CO–). Also the three peaks were observed for O (1s) at 531.43 eV (–CH2–CO–NH–), 532.99 eV (H2O) and at 534.66 eV ($–CH_2–O–$). These data

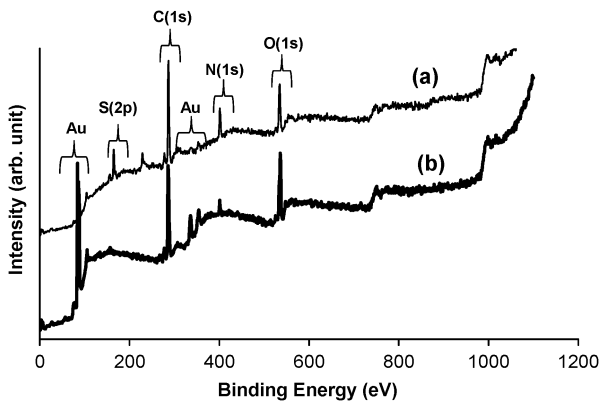

Fig. 2 Typical comparative X-ray photoelectron spectrum of (a) Au–cysteamine and (b) Au–MEODA. The spectrum for the bare Au is omitted for clarity.

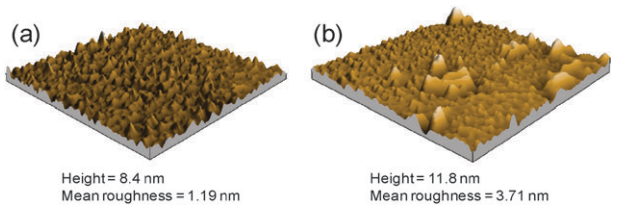

Fig. 3 Typical comparative AFM images of Au–MEODA and Au–MEODA–MA.

further confirm that the stearic acid SAM was formed onto a preformed cysteamine SAM on gold electrode.

As already shown previously,[12] the modification processes were confirmed by comparative AFM images of the bare Au and modified species. Comparative AFM topographies of the MEODA (Fig. 3a) and MEODA–MA (Fig. 3b) indicate that the MEODA–MA appeared as aggregated bundles of species. The topography of MA is in close agreement with the work of Hasegawa and co-workers,[27,28] which may be ascribed to the strong van der Waal's hydrophobic attractive forces (between the alkyl chains of the MA and MEODA) and some repulsive forces (due to the so-called 'spring-like force' generated by the longer alkyl chain of the MA that has been speculated to be responsible for the highly condensed packing of MA in the cell walls of *M. tuberculosis*[28]).

Also, it appears from the comparative 3-D AFM topographies (Fig. 3(i)) that the formation of the MEODA–MA created more spaces/pores on the electrode surface, possibly due to the displacement of some of the MEODA. Given the high molecular weight of the MA and the folding behaviour of its long alkyl chains ("W" and "Z" orientations, first referred to by Minnikin and co-workers[29]), it should perhaps not be totally surprising that the pinholes in the MEODA SAM may not be sufficient for the MA to "sit side-by-side" with MEODA without having to either (i) completely detach MEODA from the electrode or (ii) displace or collapse some of MEODA creating defect sites. Given the strong Au–S bond, the latter is the most likely to occur, forming the so-called "collapsed sites" and increasing the distance between the centers of the neighbouring pinholes.[30]

3.2 Cyclic voltammetry characterisation

Fig. 4 shows comparative cyclic voltammograms first obtained to establish the extent to which the modifiers (MEODA, MA and SAP) permit electron transport between a solution redox probe ($[Fe(CN)_6]^{4-}/[Fe(CN)_6]^{3-}$) and the underlying gold electrode. Fig. 4 shows typical comparative CV evolutions of the (a) bare Au, (b) Au–MEODA, (c) Au–MEODA–MA and (d) Au–MEODA–MA/SAP in 1 mM $[Fe(CN)_6]^{4-}/[Fe(CN)_6]^{3-}$ (PBS, pH 7.0). Note that saponin is used to block pinholes or non-specific sites on the Au–MEODA–MA prior to anti-MA antibody detection in TB serum. Each of the steps is expected to form a different surface structure that will increase the thickness of the electrode, blocking the entrance of the test redox probe solution, thereby increasing the resistance to charge-transport. The following need to be emphasized from the data: first, the respective voltammograms did not show any detectable deviations even after 20 repetitive

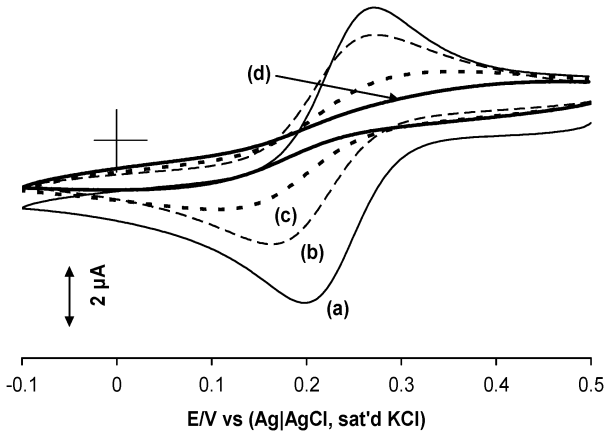

Fig. 4 Cyclic voltammograms obtained at the (a) bare Au, (b) Au–MEODA, (c) Au–MEODA–MA and (d) Au–MEODA–MA/SAP.

cyclic voltammetric scanning, indicating electrochemical stability. Second, the electrochemical kinetics, demonstrated by the peak-to-peak separation (ΔE_p), increases as bare Au ($\Delta E_p \approx 56$ mV, typical one-electron transfer kinetics) > Au–MEODA ($\Delta E_p \approx 90$ mV) > Au–MEODA–MA ($\Delta E_p >$ 160 mV) > Au–MEODA–MA/SAP ($\Delta E_p > 200$ mV). The decrease in both the ΔE_p and voltammetric peak current densities following the modification of the gold surface is a clear indication that the suppression of electron transport is strongly dependent on the thickness of the film. The changes seen in the cyclic voltammetric evolutions may be ascribed to the progression from macroelectrode (*i.e.*, planar diffusion for bare Au) to randomly-spaced microelectrode arrays or sites (*i.e.*, radial diffusion).

Compton and co-workers elegantly developed a theoretical framework for dealing with voltammetry at spatially heterogeneous electrodes.[31–33] From their work, the voltammogram of the bare Au arises from pure linear diffusion, characteristic of category 1 (naked electrode). The CVs of the modified electrodes describe the behaviour typical of ''micro-sized'' electro-active zones that are separated with inert blocking materials such that the electrode as a whole behaves like a collection of isolated microelectrodes, each of which experiencing covergent or radial diffusion that may lead to either type 2 or type 3 phenomenon. In the type 2, the diffusion layer thickness, δ, is larger than the insulating layer but not large enough to permit overlapping of neighbouring diffusion layers. In type 3, the diffusion layer thickness, δ, is larger than the insulating layer such that the neighbouring diffusion layers weakly overlap. Electrochemically, an increase in distance between microscopic sites manifests itself as an increase in the ΔE_p. Third, it is worth noting here that the long chain MEODA did not effectively block electron-transfer as one usually sees with long-chain alkylthiol SAMs.[34,35] It is well known that long-chain alkanethiol SAMs easily (even in few minutes) form highly integrated, well packed and pinhole-free SAMs on gold. This weak blockage of the electrode surface by the long-chain MEODA, even after long-hour deposition, is attributed to the spaces/pores created by the presence of the amide bond in its molecular structure, similar to that seen recently by Wilkop *et al.*[36] in their work with the disulfide-terminated hexyl thioctate SAM that contained oxo-containing moieties. Since short-chain alkylthiols SAMs are known for their loose-packing, defects and pinholes, the precursor short-chain cysteamine SAM for the MEODA should be expected to enhance the creation of the pores. We imagine that these pores within the MEODA SAMs allow for the stable integration of the MA *via* van der Waal's attractive forces, typical of long-chain alkane SAMs. Finally, unlike the bare Au and Au–MEODA that gave well defined peaked voltammograms (typical of linear/planar diffusion at macroelectrodes), Au–MEODA–MA and Au–MEODA–MA/SAP exhibit somewhat sigmoidal-shaped voltammograms (typical of radial diffusion at microelectrodes). The assumption of sigmoidal shapes indicates that electron-transfer processes take place at pinhole sites,[30,37–39] responsible for the diffusion or permeation of the solution species into the underlying electrodes (pinhole analysis is later discussed in section 3.4).

3.3 Impedimetric assessment of charge transfer dynamics

EIS provides important insights into the integrity and properties of electrochemical systems, and less perturbing (smaller applied potential ≤ 10 mV) than CV, which is particularly very crucial to soft materials studied in this work. Thus, all subsequent studies, unless otherwise stated, were performed with EIS. The EIS measurements were performed in the $[Fe(CN)_6]^{4-}/[Fe(CN)_6]^{3-}$ solution as in CV experiments (Fig. 4) at the formal potential ($E_{1/2} \approx 200$ mV). Fig. 5 shows examples of the Nyquist plots obtained for these electrodes.

An essential aspect of EIS is the ability to fit the spectral data with some theoretical electrical equivalent circuit models. As seen in Fig. 5 (and Table 1), the bare gold electrode was satisfactorily fitted with the modified Randles equivalent circuits (Fig. 6a), while the Au–MEODA, Au–MEODA–MA and Au–MEODA–MA/SAP were fitted with Randles circuits incorporating a Voigt circuit of two or three RC elements in series, equivalent circuits (Fig. 6b–d), respectively. The fitting parameters involve the electrolyte resistance (R_s), electron-transfer resistance (R_{ct}), constant phase element (CPE) due to the inherent roughness of the electrode (a real system) rather than pure double layer capacitance (C_{dl}) expected for an ideal system), and Warburg-type impedance (Z_w), which is associated with the diffusion of the ions of the redox probe. Generally, the Nyquist plots exhibited the characteristic semicircles at high frequencies and a straight line at low frequencies, corresponding to kinetic and diffusion processes, respectively.

The apparent electron-transfer rate constant (k_{app}) values of the electrodes were obtained from the eqn (1):

$$k_{app} = \frac{RT}{n^2F^2AR_pC} \quad (1)$$

where n is the number of electrons transferred (3), A is the experimentally-determined area of the electrode, R_p is effective charge transport resitance or polarization resistance obtained by the summation of the charge-transfer resistances in series connection, C is the concentration of the $[Fe(CN)_6]^{3-}$ (in mol cm^{-3}, the concentration of $[Fe(CN)_6]^{3-}$ and $[Fe(CN)_6]^{4-}$ are equal), R is the ideal gas constant, T is the absolute T/K and F is the Faraday constant. The calculated values are shown in Table 1. The k_{app} values decreases as: bare Au

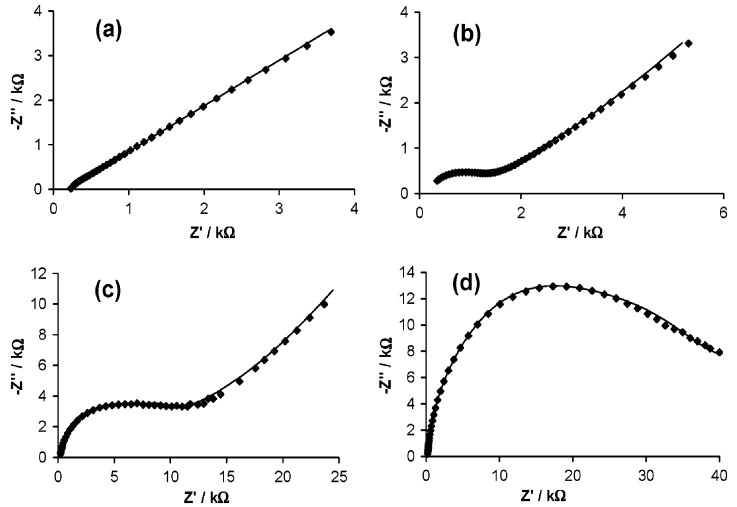

Fig. 5 Nyquist plots for the (i) bare Au, (ii) Au–MEODA, (iii) Au–MEODA–MA and (iv) Au–MEODA–MA/SAP. The symbols represent the experimental data, while solid lines are fitted curves using equivalent circuits shown in Fig. 6.

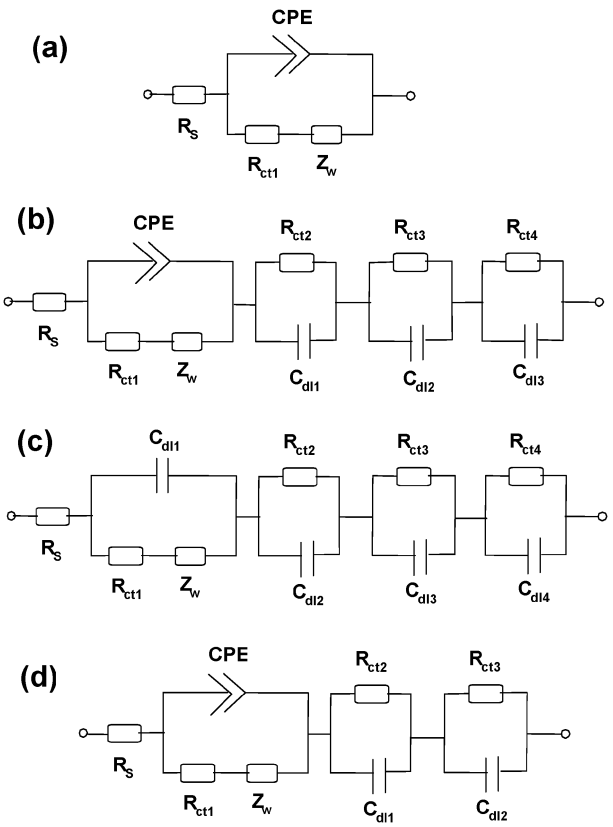

Fig. 6 Respective equivalent circuit model used to fit the impedance spectra of (a) bare Au, (b) Au–MEODA, (c) Au–MEODA–MA and (d) Au–MEODA–MA/SAP.

(4.23×10^{-2} cm^2 s^{-1}) < Au–MEODA (5.13×10^{-3} cm^2 s^{-1}) < Au–MEODA–MA (7.01×10^{-4} cm^2 s^{-1}) < Au–MEODA–MA-SAP (1.85×10^{-4} cm^2 s^{-1}) indicating that electron transfer processes between the redox probe and the underlying gold surface are made more difficult with increasing layers of modifiers, excellently corroborating the ΔE_p results from the CV experiment. The impedance of the CPE (Z_{CPE}) is defined as (eqn (2)):

$$Z_{CPE} = \frac{1}{[Q(j\omega)^n]} \quad (2)$$

where Q is the frequency-independent constant relating to the interface, $j = \sqrt{-1}$, ω is the radial frequency, the exponent n arises from the slope of log Z *vs.* log f (and has values $-1 \leq n \leq 1$). If $n = 0$, the CPE behaves as a pure resistor; $n = 1$, CPE behaves as a pure capacitor; $n = -1$ CPE behaves as an inductor; while $n = 0.5$ corresponds to Warburg impedance (Z_w) which is associated with the domain of mass transport control arising from the diffusion of ions. Generally speaking, CPE may occur as a result of several factors[40] including (i) the nature of the electrode (*e.g.*, roughness and polycrystallinity), (ii) distribution of the relaxation times due to heterogeneities existing at the electrode/electrolyte interface, (iii) porosity and (iv) dynamic disorder associated with diffusion. From Table 1, $n \geq 0.78$, meaning pseudo-capacitive behaviour. From the Bode plots (Fig. 7), the slopes of the log Z *vs.* log f plot at the mid frequency region are less than the ideal -1.0 for pure capacitive behaviour, which is indicative of pseudocapacitive behaviour.

Also, from the other Bode plot (*i.e.*,—phase angle (ϕ) *vs.* log f) the phase angles are less than the 90° expected of an ideal capacitive behaviour, confirming the pseudocapacitive behaviour.The following features shown by the comparative impedimetric data of the bare Au, Au–MEODA, Au–MEODA–MA and Au–MEODA–MA/SAP should be emphasized. First, every attempt to fit the other electrodes with the ideal or modified Randles circuit or a simple one-reaction RC time constant circuit was unsuccessful as very large fitting error values were obtained. The non-ideal behaviour of each of the semi-circular arcs of the Au–MEODA and Au–MEODA–MA and Au–MEODA–MA/SAP (*i.e.*, departure from a single arc centered on the real axis of Z') and our inability to fit these arcs by a single electrochemical reaction time constant prompted us to speculate the occurrence of a variety of

Table 1 Electrochemical impedance data obtained for the electrodes

EIS parameters	Electrode[a]			
	Bare Au	Au–MEODA	Au–MEODA–MA	Au–MEODA–MA/SAP
R_s/Ω	230.7 (0.25)	254.4 (2.86)	183 (1.98)	190.3 (1.03)
$C_{dl1}/\mu F$		2.154 (8.39)		
$CPE/\mu F$	3.27 (13.00)		0.24(3.75)	1.67 (9.91)
n	0.893 (1.48)		0.89 (0.51)	0.78 (1.00)
$R_{ct1}/k\Omega$	0.229 (10.53)	0.716 (5.21)	5.82 (3.68)	24.35 (1.41)
$Z_w/\mu\Omega^{-1}$	77.6 (0.69)	83.5 (1.34)	85.5 (2.72)	74.3 (8.77)
$R_{ct2}/k\Omega$		0.547 (5.37)	2.46 (11.42)	2.32 (16.13)
$C_{dl2}/\mu F$		0.383 (12.39)	113.4 (16.03)	0.439 (9.33)
$R_{ct3}/k\Omega$		0.628 (4.80)	3.02 (6.47)	13.05 (3.92)
$C_{dl3}/\mu F$		0.0624 (2.59)	1.23 (11.63)	268.8 (4.68)
$R_{ct4}/k\Omega$			2.57 (7.84)	12.64 (4.90)
$C_{dl4}/\mu F$			9.08 (17.92)	
$k_{app}/cm^2\ s^{-1}$	$(4.23 \pm 0.45) \times 10^{-2}$	$(5.13 \pm 0.79) \times 10^{-3}$	$(7.01 \pm 1.9) \times 10^{-4}$	$(1.85 \pm 0.48) \times 10^{-4}$

[a] The value in parenthesis represents the relative percent error obtained from fitting the impedance spectrum using the proposed equivalent circuits (Fig. 6).

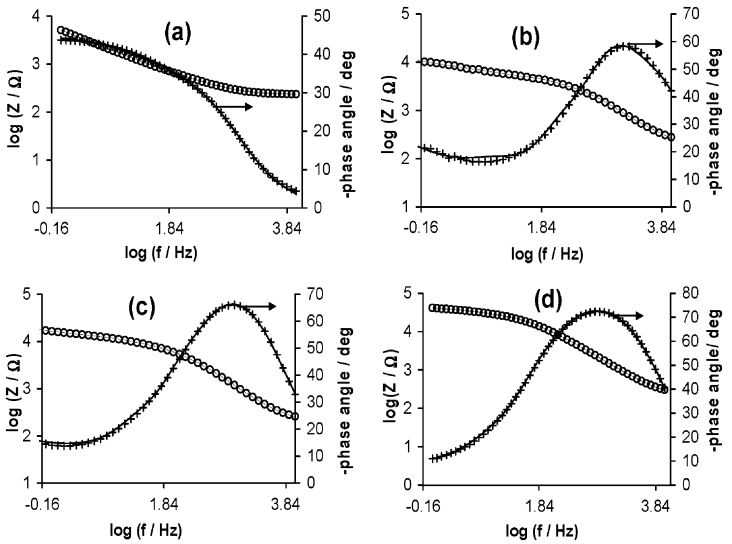

Fig. 7 Bode plots for the (i) bare Au, (ii) Au–MEODA, (iii) Au–MEODA–MA and (iv) Au–MEODA–MA/SAP. The symbols represent the experimental data, while solid lines are fitted curves using equivalent circuits shown in Fig. 6.

physico-electrochemical phenomena involving more than one RC time constants, notably, multiple or coupled reaction sequences, to roughening of the electrode, and to frequency-dependent ohmic resistances caused by non-uniform charging of the electrode/electrolyte double layer.

As is evident from the experimental impedance spectra (Nyquist (Fig. 5) and Bode plots (Fig. 7)) of the Au–MEODA, Au–MEODA–MA and Au–MEODA–MA/SAP exhibited excellent fitting with equivalent electrical circuit models involving Voigt circuit of two or more RC elements in series with the Randles circuit, confirming that the impedance data are influenced by distributed-time-constant phenomena.[14] Simply stated, each of these semi-circular arcs comprised overlapping arcs due to the close proximity of time constants. These time constants are so close that it is even impossible to observe them as more than one peak in their respective Bode plots. Second, impedance spectra are known to contain features that could be directly related to microstructures, with the grain boundary phases of microstructures having a dominant blocking effect on the impedance spectra.[13,14] As seen from Table 1, the use of the "ideal" double layer (C_{dl}) rather than CPE (which is an acceptable real practical situation) led to a more satisfactory fitting (signified by the fitted line and % relative errors).

Since electron transport processes occurring *via* permeation of the redox probe through the spaces created by the assembled species are expected to be faster than that arising through the layers,[41] we may therefore associate the Randles circuit component of the equivalent circuits to processes that occur through the spaces amongst the self-assembled molecular layers, while the Voigt elements (R_{ct2}/C_{dl2}, R_{ct3}/C_{dl3} and R_{ct4}/C_{dl4}) are attributed to the electron transfer and specific capacity of the interface arising from the collapsed sites and/or the grain boundaries within the film structure. This is in agreement with the proposal by Finklea *et al.*[38] that there are sites at which the redox couple can approach the underlying electrode surface more closely but not able to come into contact with it.

Third, it is known that time-constant (or frequency) dispersion leading to CPE behaviour occurs as a result of distribution of time constants along either the area of the electrode surface (involving a 2-dimensional aspect of the electrode) or along the axis normal to the electrode surface (involving a 3-dimensional surface).[42] One of the recognized sources of 2-D distribution is surface heterogeneities (such as grain boundaries, crystal faces of polycrystalline electrode, or other variations in surface properties), whereas 3-D distribution is usually associated with changes in the conductivity of oxide layers or from porosity or surface roughness.[43] Importantly, unlike a 3-D distribution, a 2-D distribution shows an ideal RC behaviour, meaning that impedance measurements are very useful in distinguishing whether the observed global CPE behaviour is due to a 2-D distribution, from a 3-D distribution, or from combined 2-D and 3-D distributions.[42] We may therefore conclude that the observed impedimetric behaviour of the Au–MEODA is due mainly to 2-D distribution while those of the Au–MEODA–MA is a combination of 2-D and 3-D distributions. Note that despite the fitting of the spectra with an ideal RC element, the phase angles seen on the Bode plots deviate from the ideal -90° expected of a pure RC, which further confirms that the presence of the 2-D distribution arises from CPE behaviour. The microstructure model is a complex model that has been a subject of extensive mathematical theories.[13] Some of the well known microstructural systems that exhibit grain/grain boundary impedance spectra include oxides and liposomes. Thus, at the moment, it may be reasonable to speculate that the self-assembled MEODA, MEODA–MA and MEODA–MA/SAP species exhibit microstructural behaviour with the relaxations (time-constants) corresponding to possible orientations of these microstructures.

3.4 Impedimetric assessment of structural disorder

Returning to the discussion on pinholes, an important parameter to probe the adsorption kinetics of monolayers by electrochemical method is the fractional coverage (θ). The presence of pinholes or defect sites on redox-inactive SAMs (responsible for the diffusion or permeation of the solution species into the underlying electrodes), as in this work, is the consequence of disorderly-packed SAMs, and are best interrogated using EIS techniques. As has elegantly been described by Tong and co-workers,[34,44] these defect sites may arise *via* any of the three possible ways (Fig. 8): (i) the well-oriented domain; (ii) the grain boundaries or steps in the gold substrate; (iii) the monolayer "collapsed site", a concept first proposed by Finklea *et al.*,[38] which could occur when the packing of organothiolate SAM on gold substrate is incomplete within a localized spot, leading to the long-chain alkyl chain folding over the defect; and finally (iv) *via* the monolayer grain boundary between two monolayer domains with different orientations of tilt angles. The extent to which these defects occur determine the thickness and degree of molecular order of the immobilized species. If the SAMs do not contain pinhole defects, it means that the only way by which the electron transfer process can occur is by electron-tunneling across the redox-inactive insulating barrier (*i.e.*, thin layers at

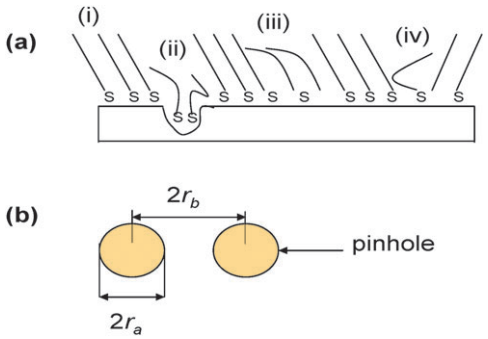

Fig. 8 (A) Cartoon representation of the (a) possible defect sites associated with gold electrodes modified with alkanethiolate monolayer. (i) Well-oriented domain; (ii) Au substrate grain boundary; (iii) monolayer collapsed site; and (iv) monolayer grain boundary. (b) is the pinhole model.

collapsed sites or thick layers in well-assembled domains). Assuming that electron-transfer processes occur only at the bare spots of the electrodes and that diffusion of the redox probe to these defect sites is planar, the apparent fractional coverage (θ_{app}) of the modifier could be estimated from eqn (3):[45,46]

$$\theta_{app} = 1 - \left(\frac{R_{ct}^{Au}}{R_{ct}^{SAM}}\right) \quad (3)$$

where θ_{app} is the fractional coverage of the surface, R_{ct}^{Au} and R_{ct}^{SAM} are the charge transfer resistance of the bare gold and the self assembled monolayer modified gold surface, respectively.

When using eqn (3) to calculate the coverage, we found that $\theta_{app} > 0.9$. However, according to Amatore *et al.*,[30] eqn (3) is not appropriate for describing fractional coverage if $\theta_{app} > 0.9$. In this case, we employed another model that takes cognizance of radial diffusion or microelectrode array behaviour, radial size of the pore/pinhole and their distribution in the SAM , eqn (4):[47]

$$\theta_{app} = 1 - \left(\frac{\sigma_W}{m - \sigma_W}\right) \quad (4)$$

where σ_W is the Warburg coefficient (225.3 Ωs^{-1} cm^2) calculated for the clean bare gold electrode *via* the slope of the linear Z' *vs.* $\omega^{-1/2}$ plot obtained in the low frequencies region (Fig. 9a), while m is the slope of the linear interval in the high frequency regions of the Z' *vs.* $\omega^{-1/2}$ (Fig. 9b–d) function obtained at the respective modified electrodes. Thus, using eqn (5), the θ_{app} values for the Au–MEODA, Au–MEODA–MA and Au–MEODA–MA/SAP were essentially the same (*ca.* 0.97). The radius of the pinhole (r_a) was estimated using eqn (5):[48]

$$r_a^2 = \frac{D}{0.36q} \quad (5)$$

where D is the diffusion coefficient of the redox couple, assuming $D_o \approx D_r \approx 7.6 \times 10^{-6}$ cm^2 s^{-1},[33] and q is the so-called "transition radial frequency", corresponding to the turning point between the high- and low-frequency domains in the Z' *vs.* $\omega^{-1/2}$ plots, which can be determined from the maximum in the Z'' *vs.* $\omega^{-1/2}$ plot of the respective modified

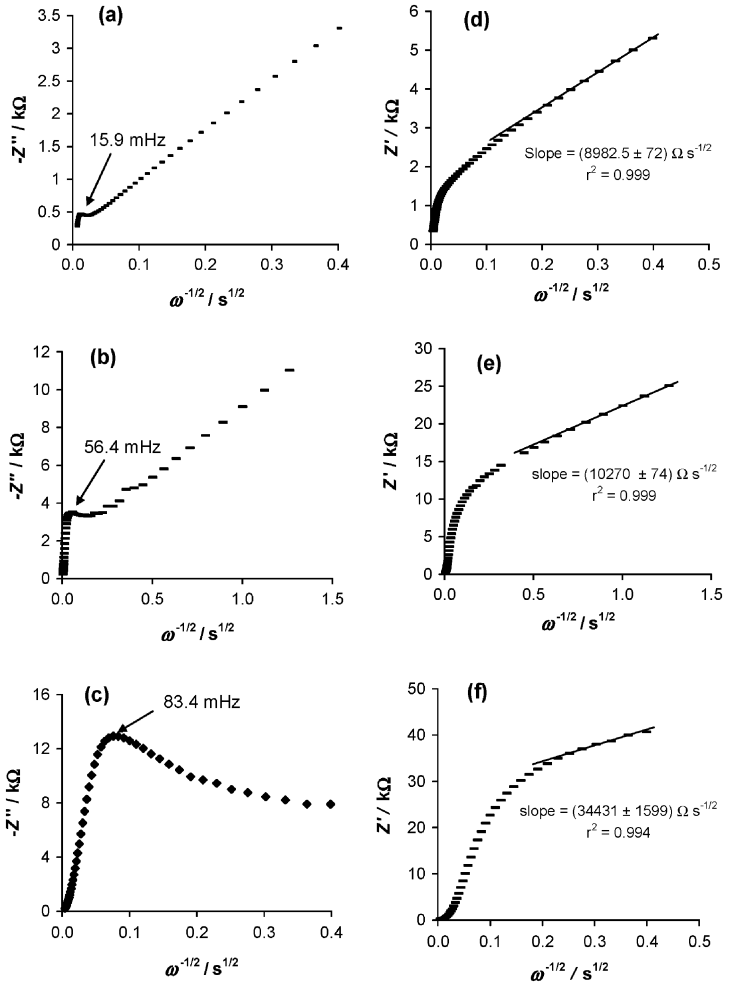

Fig. 9 Plots of Z' *vs.* $\omega^{-1/2}$ (left panel, a–d) and Z'' *vs.* $\omega^{-1/2}$ (right panel, a′–d′) of the bare Au (a, a′), Au–MEODA (b, b′), Au–MEODA–MA (c, c′) and Au–MEODA–MA/SAP (d, d′).

bare Au electrodes (Fig. 9b–d) using eqn (6):[39]

$$\omega = \frac{q}{2} \tag{6}$$

The radius of the inactive domain surrounding the micro-electrode (r_b, *i.e.*, half the distance between the centers of the neighbouring pinholes) is obtained from eqn (7) as:[38,47]

$$1 - \theta_{app} = \frac{r_a^2}{r_b^2} \tag{7}$$

Fig. 10 is a plot of the r_a and r_b*vs.* the modified electrodes. From the Fig. 10, the r_a values are almost independent of the modifier, they increased slightly from the Au–MEODA (0.84 μm) to Au–MEODA–MA (1.73 μm) and to the Au–MEODA–MA/SAP (3.50 μm) compared to their r_b counterparts that increased from Au–MEODA (4.68 μm) to Au–MEODA–MA (10.69 μm) and to the Au–MEODA–MA/SAP (41.98 μm). According to literature,[21,47,48] such insignificant increase in the r_a values suggests transformation of some pinholes to collapsed sites, while the significant increase in the r_b values indicates the disappearance of some of the original pinholes. Simply stated, in the MEODA SAM, for instance, MA could bind to some pinhole defect sites of the

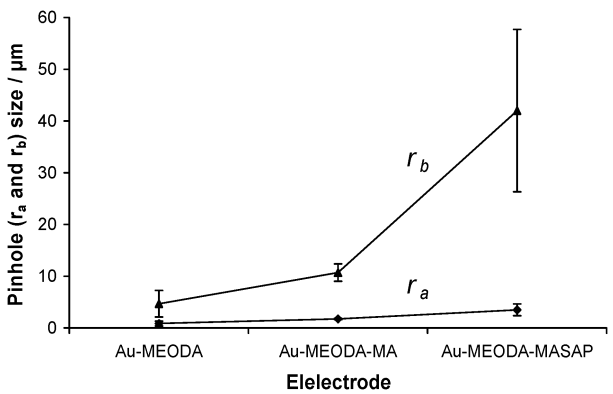

Fig. 10 Comparative plots of the r_a and r_b of the Au–MEODA, (ii) Au–MEODA–MA and (iii) Au–MEODA–MA/SAP.

MEODA and make them disappear, thereby increasing the pinhole separation. If electron-tunneling across an insulating barrier is involved in electron transfer process, then the redox current at any potential should decrease exponentially with the barrier thickness according to eqn (8):[35,49]

$$I = I_0 e^{-\beta d} \tag{8}$$

where I_0 is the current obtained at the bare gold electrode, β is the electron-tunnelling coefficient (β = 1.05 per methylene group[50]), and d is the thickness of the monolayer film. Under equilibrium conditions, eqn (8) may be expressed as eqn (9):[35]

$$k = k_0 e^{-\beta d} \quad (9)$$

where k_0 and k are the standard electron transfer rate constants at the bare and film-modified gold electrodes, respectively.

Given that eqn (9) implies that the electron transfer constant at a thick film is much less than that across a thin film, it is possible to compare the theoretical and experimental electron transfer rate constants to determine the existence of collapsed sites. If the apparent electron transfer rate constant (k_{app}) obtained from the Au–MEODA (experimental value) is much larger than the theoretical electron transfer rate constant, we can conclude that collapsed sites do really exist in the MEODA, and most certainly in MEODA–MA and MEODA–MA/SAP. The k_{app} values were determined as before using eqn (2). For an ideal Au–MEODA SAM (*i.e.*, free of collapsed sites, all MEODA species standing upright), d is a 21-methylene group long (*i.e.*, assuming a 2-methylene for the amide bond). If we assume k_0 = 0.031 cm s^{-1} for the $[Fe(CN)_6]^{3-/4-}$ redox system,[31–33,49] and applying eqn (9), k is calculated as 8.23 × 10^{-12} cm s^{-1}. Since this theoretical value is about 9 orders of magnitude lower than the k_{app} of 5.13 × 10^{-3} cm s^{-1} for Au–MEODA, it clearly confirms the existence of collapsed sites at the Au–MEODA and that, in addition to the direct permeation of the redox probe into the active sites of the bare gold electrode, electron tunneling through the films or collapsed, "down-lying" MEODA and MA molecules contribute to the observed Faradaic current.

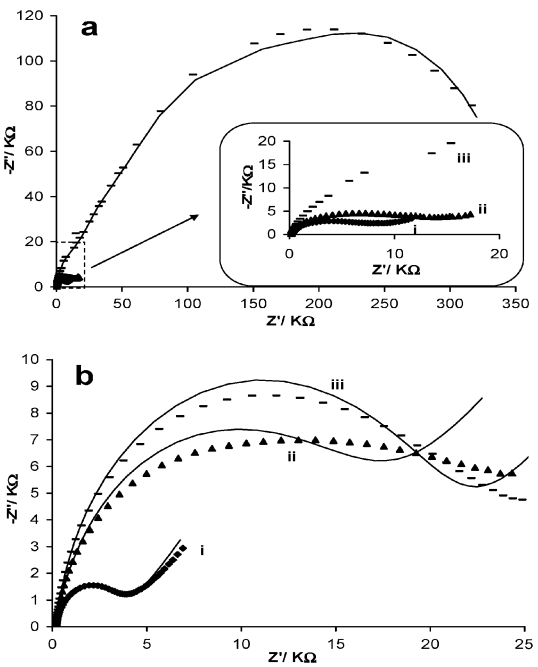

Fig. 11 (a) Typical Nyquist plots for the Au–MEODA–MA/SAP before (i) and after (iii) incubation in TB^+ serum. (ii) is the control experiment of the same TB^+ serum. (b) Nyquist plots for the Au–MEODA–MA/SAP before (i) and after (iii) incubation in TB^- serum. (ii) is the control experiment of the same TB^- serum. The symbols represent the experimental data, while solid lines are fitted curves. Fig. a (iii) was fitted with circuit shown in Fig. 12, while other spectra were fitted with circuit shown in Fig. 6d.

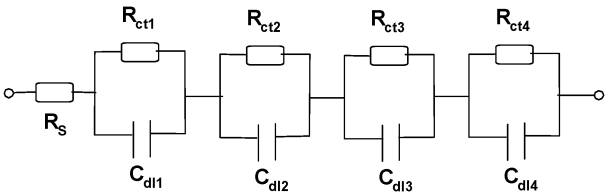

Fig. 12 Equivalent circuit model used to fit the impedance spectrum of Au–MEODA–MA/SAP upon interaction with the HIV^+TB^+ serum.

3.5 Impedimetric assessment of the MA/anti-MA antibody interactions

One of the main advantages of EIS as an electroanalytical tool is its sensitivity to structure, be that the structure of a solid or a liquid.[43]Fig. 11a exemplifies typical EIS evolutions (Nyquist plots) obtained at a constant serum dilution (1 : 1000) for the Au–MEODA–MA/SAP before (i) and after (iii) incubation in TB+ serum. (ii) is the control experiment of the same TB+ serum. Fig. 11b demonstrate typical EIS Nyquist plots for the Au–MEODA–MA/SAP before (i) and after (iii) incubation in TB^- serum. (ii) is the control experiment of the same TB^- serum. As expected, the TB+ serum exhibits more blocking behaviour towards the Au–MEODA–MA/SAP electrode compared to others. Upon interaction of the Au–MEODA–MAP/SAP with the HIV^+TB^+ serum, the spectrum was best fitted with a Voigt circuit model comprising four RC elements in series (Fig. 12), which is characteristic of blocking/inhibition behaviour, with a solution resistance (R_s), confirming that the impedance data are influenced by distributed-time-constant phenomena. In other words, the poorly resolved arc observed at the TB positive serum comprised overlapping arcs due to the close proximity of time constants. This is further confirmed from the Bode plots (Fig. 5b and d), where four peaks correspond to four relaxation processes (72.9° at 1995 Hz, 72.8° at 316 Hz, 50.1° at 10 Hz and 35.4° at 0.63 Hz). On the contrary, the control experiments as well as the HIV^-/TB^- serum were fitted with the same circuit as for the Au–MEODA–MA/SAP (Fig. 6d), clearly indicating that diffusion still occurs at this electrode using the control experiment and HIV^-/TB^- serum solutions.

Although the double layer (C_{dl1}–C_{dl4}) was used in the fitting circuit, the phase angles were $<90°$, meaning that the $C_{dl} \approx$ CPE.[14] It may thus be concluded that the observed impedimetric behaviour of the HIV^+TB^+ serum arise mainly from a 2-D distribution. Unlike the other electrodes, the relaxations are more discernible in the Bode plots (Fig. 13).

Thus, we may speculate that the formed biocomplex (MA-anti-MA antibody in TB positive serum) as seen in Fig. 11 exhibits microstructural behaviour. The EIS data are summarised in Table 2. The values of polarization resistance at the Au–MEODA–MA/SAP electrode incubated in TB positive serum (294 kΩ) is about 18 times higher than those of the electrodes incubated in the TB-negative serum (16 kΩ)

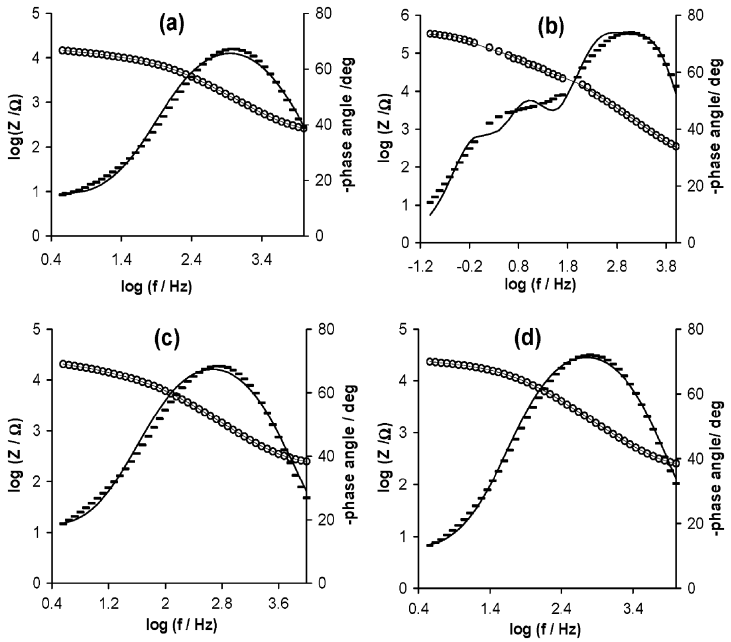

Fig. 13 Bode plots for the same experiments in Fig. 11. The symbols represent the experimental data, while solid lines are fitted curves; (b) was fitted with the circuit shown in Fig. 12, while the other spectra were fitted with the circuit shown in Fig. 6d.

Table 2 Electrochemical impedance data obtained for the Au–MEODA–MA/SAP electrode upon interaction with TB^+/HIV^+ serum

EIS Parameters	Au–MEODA–MA/SAP-serum[a]
R_s/Ω	198.2 (7.09)
CPE/nF	208 (11.9)
$R_{ct1}/k\Omega$	0.761 (28.3)
$R_{ct2}/k\Omega$	73.8 (6.75)
C_{dl}/nF	460 (6.61)
$R_{ct3}/k\Omega$	19.42 (6.68)
C_{dl3}/nF	109 (5.28)
$R_{ct4}/k\Omega$	230.9 (4.15)
C_{dl4}/nF	163.4 (8.97)

[a] Value in parenthesis is the relative percent error from fitting using circuit in Fig. 12.

or the electrodes that did not undergo any incubation in either of the TB-positive or negative serum (4 kΩ). This simply means that electron transfer between the redox probe and the gold substrate is most inhibited following interaction of the electrode with the anti-MA antibodies present in the TB positive serum.

Note that the main difference between the equivalent electrical circuit used to fit the TB positive spectrum (Table 2) and others (Table 1) is the absence of the Warburg (Z_w) element, indicating an efficient blockage of diffusion of the redox probe ions. It also confirms the presence of anti-MA antibodies in the human serum and interaction of these antibodies with the immobilized MAs. This result suggests that the mechanism underlying the interaction of the MA-modified electrode with the TB positive serum is the formation of an electrode that acts as an ionic insulator that is virtually defect-free, capable of strongly suppressing the penetration of the redox probe into the underlying gold electrode (Scheme 2).

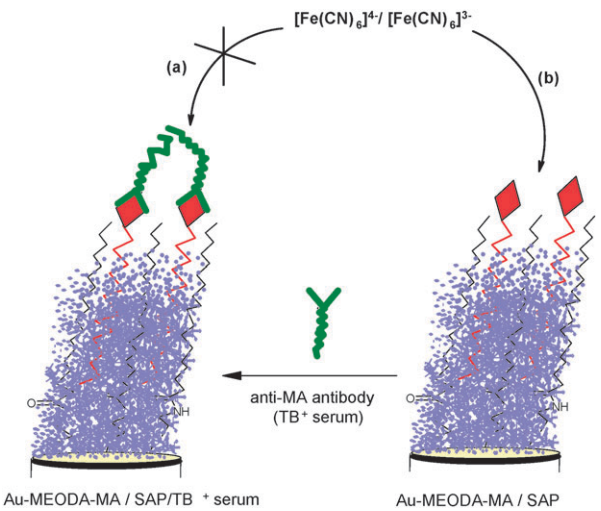

Scheme 2 Schematic of the interaction of anti-MA antibodies in the TB+ serum, also showing cartoon of the mechanism of the suppression (step a) and penetration (step b) of the redox probe into the underlying gold electrode.

Conclusions

The integrity and properties of the mycolic acids integrated into *N*-(2-mercaptoethyl)octadecanamide (MEODA) monolayer have been evaluated and compared using AFM, cyclic voltammetry and electrochemical impedance spectroscopy. Results showed that MA-modified gold substrate behaves as microelectrode arrays which permit electron transport between a redox-active probe in solution and the underlying gold surface. TB-antibodies present in HIV-infected human sera strongly interact with the modified MA showing rather a

compact and stable complex structure. Three remarkable findings in the EIS study that should be emphasized are: first, the MEODA and MA modified electrodes as well as the interaction between immobilized MA and anti-MA antibody in TB positive serum typified the behaviour of microstructural systems with grain/grain boundary phases. Second, the immobilised MA and its anti-MA antibody interaction exhibited time-constant dispersion behaviour and that the distribution of these time-constants occurred mainly along the area of the electrode (*i.e.*, 2-D distributions arising from surface heterogeneities such as the grain boundaries) with some contributions from the axis normal to the plane of the electrode surface (*i.e.*, 3-D distribution (arising from porosity of the electrode). Finally, the change in electrode polarization resistances in TB positive sera are approximately 10 times larger than those observed in the TB negative sera, which suggests that the proposed TB immunosensor can satisfactorily discriminate between positive and negative TB sera.

The crucial physico-electrochemical insights into the behaviour of surface-confined MA, provided in this work, should form a useful basis for the design and development of potential impedimetric immunosensing platforms using, not only the investigated molecular species, but other molecules for developing relevant immunosensing platforms. We feel that this work has laid some foundation and opened up new questions to be further investigated. Such future studies should include the exploration of the impact of different immobilization strategies and organothiolate SAM species as viable hydrophobic supports for MA; impact of serum samples with different levels of antigens; impact of different redox probes; employment of different human TB positive sera and controls; and applicability of cost-effective and easy-to-use one-shot electrodes for monitoring progress in TB treatment, especially the drug-resistant TB. All these should constitute the main thrust of future investigations.

Acknowledgements

We thank CSIR, NRF (GUN # 2073666, 65305, 68338, 45489), EDCTP (CT.2004.32040.001) and Cape Biotech/Lifelab for their support. NSM thanks NRF for MSc bursary. JP thanks MinTEK and NRF for PhD bursaries/scholarships.

References

1 D. E. Minnikin, S. M. Minnikin and G. Dobson, *J. Gen. Microbiol.*, 1983, **129**, 889.
2 G. K. Schleicher, C. Feldman, Y. Vermaak and J. A. Verschoor, *Clin. Chem. Lab. Med.*, 2002, **40**, 882.
3 S. T. Thanyani, V. Roberts, D. G. R. Siko, P. Vrey and J. A. Verschoor, *J. Immunol. Methods*, 2008, **332**, 61.
4 *Global Tuberculosis Control: Epidemiology, Strategy, Financing*, WHO2009 Report, Switzerland.
5 E. L. Corbett, C. J. Watt, N. Walker, D. Maher, B. G. Williams, M. C. Raviglione and C. Dye, *Arch. Intern. Med.*, 2003, **163**, 1009.
6 I. K. R. U. Devi, B. Ramalingam and A. Raja, *Diagn. Microbiol. Infect. Dis.*, 2003, **46**, 205.
7 R. G. Nuzo and D. L. Allara, *J. Am. Chem. Soc.*, 1983, **105**, 4481.
8 A. Hatzor, T. van der Boom-Moav, S. Yochelis, A. Shanzer and I. Rubinstein, *Langmuir*, 2000, **16**, 4420.
9 H. Doron-Mor, A. Hatzor, A. Vaskevich, T. van der Boom-Moav, A. Shanzer and I. Rubinstein, *Nature*, 2000, **406**, 382.
10 B. O. Agboola and K. I. Ozoemena, *Phys. Chem. Chem. Phys.*, 2008, **10**, 2399.
11 D. Nkosi and K. I. Ozoemena, *J. Electroanal. Chem.*, 2008, **621**, 304.
12 N. S. Mathebula, J. Pillay, G. Toschi, J. A. Verschoor and K. I. Ozoemena, *Chem. Commun.*, 2009, 3345.
13 *Impedance Spectroscopy: Theory Experiment, and Applications*, ed. E. Barsoukov and J. R. Macdonald, Wiley, Hoboken, New Jersey, 2nd edn, 2005, ch. 1–4.
14 M. E. Orazem and B. Tribollet, *Electrochemical Impedance Spectroscopy*, John Wiley & Sons Inc., Hoboken, NJ, 2008.
15 J. Pillay and K. I. Ozoemena, *Electrochim. Acta*, 2009, **54**, 5053.
16 J. Pillay, B. O. Agboola and K. I. Ozoemena, *Electrochem. Commun.*, 2009, **11**, 1292.
17 A. G. Mantzila, V. Maipa and M. I. Podromidis, *Anal. Chem.*, 2008, **80**, 1169.
18 A. V. Pournaras, T. Koraki and M. I. Prodromidis, *Anal. Chim. Acta*, 2008, **624**, 301.
19 M. A. Goodrum, D. G. R. Siko, T. Niehues, D. Eichelbauer and J. A. Verschoor, *Microbios*, 2001, **106**, 55.
20 D. Nkosi and K. I. Ozoemena, *Electrochim. Acta*, 2008, **53**, 2782.
21 P. Diao, M. Guo and R. Tong, *J. Electroanal. Chem.*, 2001, **495**, 98.
22 J. J. Gooding, R. Wibowo, J. Liu, W. Yang, D. Losic, S. Orbons, F. J. Meams, J. G. Shapter and D. B. Hibbert, *J. Am. Chem. Soc.*, 2003, **125**, 9006.
23 Y. Benadie, M. Deysel, D. G. R. Siko, V. V. Roberts, S. Van Wyngaardt, S. T. Thanyani, G. Sekanka, A. M. C. Ten Bokum, L. A. Collett, J. Grooten, M. S. Baird and J. A. Verschoor, *Chem. Phys. Lipids*, 2008, **152**, 95.
24 *Handbook of X-Ray Photoelectron Spectroscopy*, ed. G. E. Muilenberg, Perkin-Elmer Corp., Eden Praire, Minnesota, 1979.
25 D. G. Castner, K. Hinds and D. W. Grainger, *Langmuir*, 1996, **12**, 5083.
26 J. Chattopadhyay, F. de Jesus Cortez, S. Chakraborty, N. K. H. Slater and W. E. Billups, *Chem. Mater.*, 2006, **18**, 5864.
27 T. Hasegawa, J. Nishijo and M. Watanabe, *Langmuir*, 2000, **16**, 7325.
28 T. Hasegawa, S. Amino, S. Kitamura, L. Matsumoto, S. Katada and J. Nisgijo, *Langmuir*, 2003, **19**, 105.
29 G. Sekanka, M. Baird, D. Minnikin and J. Grooten, *Expert Opin. Ther. Pat.*, 2007, **17**, 315.
30 C. Amatore, J. M. Saveant and D. Tessier, *J. Electroanal. Chem.*, 1983, **147**, 39.
31 T. J. Davies and R. G. Compton, *J. Electroanal. Chem.*, 2005, **585**, 63.
32 T. J. Davies, C. E. Banks and R. G. Compton, *J. Solid State Electchem.*, 2005, **9**, 797.
33 R. G. Compton and C. E. Banks, *Understanding Voltammetry*, World Scientific Publishing Co., Singapore, 2007.
34 X. Cui, D. Jiang, P. Diao, J. Li, R. Tong and X. Wang, *J. Electroanal. Chem.*, 1999, **48**, 243.
35 P. Diao, D. Jiang, X. Cui, D. Gu, R. Tng and B. Zhong, *J. Electroanal. Chem.*, 1999, **464**, 61.
36 T. Wilkop, D. Xu and Q. Cheng, *Langmuir*, 2007, **23**, 1403–1409.
37 E. Sabatini and H. O. Finklea, *J. Phys. Chem.*, 1987, **91**, 6663.
38 H. O. Finklea, S. Avery, M. Lynch and T. Furtsch, *Langmuir*, 1987, **3**, 409.
39 K. Tokuda, T. Gueshi and H. Matsuda, *J. Electroanal. Chem.*, 1971, **102**, 41.
40 T. C. Girija and M. V. Sangaranarayanan, *J. Appl. Electrochem.*, 2006, **36**, 531.
41 J.-Y. Park, Y.-S. Lee, B. H. Kim and S.-M. Park, *Anal. Chem.*, 2008, **80**, 4986.
42 M. E. Orazem and B. Tribollet, *Electrochemical Impedance Spectroscopy*, John Wiley & Sons Inc., Hoboken, NJ, 2008, ch. 13.
43 N. Bonanos, B. C. L. Steele and E. P. Butler, in *Impedance Spectroscopy: Theory Experiment, and Applications*, ed. E. Barsoukov

and J. R. Macdonald, Wiley, Hoboken, New Jersey, 2nd edn, 2005, ch. 4.
44 L. V. Protsailo and W. R. Fawcett, *Electrochim. Acta*, 2000, **45**, 3497.
45 H. O. Finklea, D. A. Snider, J. Fedyk, E. Sabatani, Y. Gafni and I. Rubinstein, *Langmuir*, 1993, **9**, 3660.
46 D. Hobara, T. Sasaki, S. I. Imabashi and T. Kakiuchi, *Langmuir*, 1999, **15**, 5073.
47 S. Campuzano, M. Pedrero, C. Montemayor, E. Fatas and J. M. Pingarron, *J. Electroanal. Chem.*, 2006, **586**, 112.
48 D. Garcia-Raya, R. Madueno, J. M. Sevilla, M. Blazquez and T. Pineda, *Electrochim. Acta*, 2008, **53**, 8026.
49 J. Xu, H. L. Li and Y. Zhang, *J. Phys. Chem.*, 1993, **97**, 11497.
50 V. Marecek, Z. Samec and J. Weber, *J. Electroanal. Chem.*, 1978, **94**, 169.